# Transcranial real-time *in vivo* recording of electrophysiological neural activity in the rodent brain with near-infrared photoacoustic voltage-sensitive dye imaging

Jeeun Kang[a], Haichong K. Zhang[a], Shilpa D. Kadam[b], Julie Fedorko[c], Heather Valentine[c], Adarsha P. Malla[f], Ping Yan[d], Jin U. Kang[a], Arman Rahmim[c], Albert Gjedde[c,e], Leslie M. Loew[d], Dean F. Wong[c,e,f,g,h], Emad M. Boctor[a,c,1]

[a] Whiting School of Engineering, Johns Hopkins University, Baltimore, MD 21218, USA

[b] Department of Neurology, Hugo W. Moser Research Institute at Kennedy Krieger, Johns Hopkins Medical Institutions, Baltimore, MD 21205, USA

[c] Russell H. Morgan Department of Radiology and Radiological Science, Johns Hopkins Medical Institutions, Baltimore, MD 21287, USA

[d] Department of Cell Biology, University of Connecticut Health, Farmington, CT 06030, USA

[e] Department of Neuroscience, University of Copenhagen, Copenhagen 2200, Denmark

[f] Solomon H. Snyder Department of Neuroscience, Johns Hopkins Medical Institutions, Baltimore, MD 21205, USA

[g] Department of Psychiatry and Behavioral Sciences, Johns Hopkins Medical Institutions, Baltimore, MD 21287, USA

[h] Department of Neurology, Johns Hopkins Medical Institutions, Baltimore, MD 21205, USA.

[1] Corresponding author: Emad M. Boctor, PhD, Johns Hopkins Medical Institutions, 601 N. Caroline St., Baltimore, MD 21287; Office: +1 (443) 287-2975; Email: eboctor1@jhmi.edu

**Abstract**

Minimally-invasive monitoring of electrophysiological neural activities in real-time—that would enable quantification of neural functions without a need for invasive craniotomy and the longer time constants of fMRI and PET—presents a very challenging yet significant task for neuroimaging. We present *in vivo* proof-of-concept results of transcranial photoacoustic (PA) imaging of chemoconvulsant seizure activity in the rat brain. The framework involves use of a fluorescence quenching-based near-infrared voltage-sensitive dye (VSD) delivered through the blood-brain barrier (BBB), opened by pharmacological modulation of adenosine receptor signaling. Using normalized time-frequency analysis on temporal PA sequences, the neural activity in the seizure group was distinguished from those of the control groups. Electroencephalogram (EEG) recording confirmed the changes of severity and frequency of brain activities, induced by chemoconvulsant seizures of the rat brain. The findings demonstrate that PA imaging of fluorescence quenching-based VSD is a promising tool for *in vivo* recording of deep brain activities in the rat brain, thus excluding the need of invasive craniotomy.

**Keywords:** photoacoustics; transcranial; brain imaging; near-infrared voltage-sensitive dye; chemoconvulsant seizure; rat brain;

## Introduction

The quantification and monitoring of brain function is a major goal of neuroscience and research into the underlying mechanisms of the working brain.[1-5] Towards this objective, several modalities have been introduced for the purpose of appropriate neuroimaging; however, existing methods have limitations. Positron emission tomography (PET) provides high molecular resolution and pharmacological specificity, but suffers from low spatial and temporal resolution.[6-8] Functional magnetic resonance imaging (fMRI) provides higher spatial resolution of brain activity; however, the record is a complex blood-oxygenation level dependent (BOLD) signal with comparatively low temporal resolution and uncertain interpretation. [9,10] Optical imaging approaches have been used to monitor the brain function of small animals but have limited dynamic ranges and cover only superficial tissue depths because of light scattering and absorbance during penetration of biological tissue *in vivo*.[11,12] These approaches require invasive craniotomy, with problematic long-term consequences such as dural regrowth, greater likelihood of inflammatory cascade initiation, and lack of practicality of translation to non-human primate and ultimately to human studies, including those for neuropsychiatric disorders.[13] In addition, real-time imaging simultaneously with deep penetration has not been demonstrated. Near-infrared spectroscopy (NIRS) non-invasively monitors brain function in real-time (~ 1ms) for deep biological tissues (~several mm), but suffers from poor spatial resolution (~ 1 cm) at those depths.[14,15] Therefore, minimally-invasive monitoring of electrophysiological brain activities in real-time remains a task at hand in neuroimaging, with the aim to quantify brain functions at

high spatial resolution in the depths of brain tissue, without need for invasive craniotomy.

To overcome the current challenges, photoacoustic (PA) imaging has been investigated as a promising hybrid modality that provides the molecular contrast of brain function with acoustic transcranial penetration and high spatial resolution.[16,17] In PA imaging, radio-frequency (RF) acoustic pressure is generated, depending on the thermo-elastic property and light absorbance of a target illuminated by pulsed laser, and it is detected by an ultrasound transducer. Based on this mechanism, several studies have presented the capability of transcranial PA imaging. [18-20] Additionally, several PA approaches have been recently applied to detect electrophysiological brain activities in both tomographic and microscopic imaging modes; Deán-Ben et al. presented *in vivo* whole brain monitoring of zebrafish using real-time PA tomography of a genetically encoded calcium indicator, GCaMP5G.[21] Ruo et al. reported PA imaging *in vivo* of mouse brain responses to electrical stimulation and 4-aminopyridine-induced epileptic seizures by means of hydrophobic anions such as dipicrylamine (DPA).[22] However, these studies used voltage sensing in the visible spectral range (488 nm and 530 nm for GCaMP5G; 500 nm and 570 nm for DPA), which is not suitable for recording deep tissue neural activity because of the  significant optical attenuation by blood.

Here, we present transcranial recording of electrophysiological neural activity *in vivo* with near-infrared PA voltage-sensitive dye (VSD) imaging during chemoconvulsant seizures in the rat brain with intact scalp. As a step towards minimally-invasive external imaging in primates and human brains, the results demonstrate that PA imaging of

fluorescence quenching-based VSD is a promising approach to the recording deep brain activities in rat brain, without need for craniotomy.

## Methods

**Photoacoustic imaging setup.** For the recording of electrophysiological brain activities *in vivo*, real-time PA data acquisition system was built; an ultrasound research system was utilized that consisted of ultrasound linear array transducer (L14-5/38) connected to a real-time data acquisition system (SonixDAQ, Ultrasonix Medical Corp., Canada). The center frequency of the transducer was 7.1 MHz to obtain the sensing depth for neural activities in a deep brain tissue. To induce the PA signals, pulsed laser light was generated by a second-harmonic (532 nm) Nd:YAG laser pumping an optical parametric oscillator (OPO) system (Phocus Inline, Opotek Inc., USA). The tunable range of the laser system was 690-900 nm and the maximum pulse repetition frequency was 20 Hz. The laser pulse was delivered into the probe through bifurcated fiber optic bundles, each 40 mm long and 0.88 mm wide (Fig. 1a). The customized, 3-D printed shell fixes the PA probe between the outlets of the bifurcated fiber optic bundles for evenly distributed laser energy density in lateral direction on rat scalp surface. The alignment of outlets was focused specifically at 20 mm depth. The PA probe was located at around the Interaural 11.2 mm and Bregma 2.2 mm to obtain the cross-section of motor cortexes (Fig. 1c). The distance between PA probe and rat skin surface was 20 mm, and the resultant energy density was at 3.5 $mJ/cm^2$ ,which is far below the maximum permissible exposure (MPE) of skin to laser radiation by the ANSI safety standards. [23] A wavelength of 790 nm was used, at which the light energy was sufficiently absorbed by

the near-infrared VSD, i.e., IR780. Probing at this wavelength avoided the undesired time-variant change of oxygen saturation, being at the isosbestic point of Hb and $HbO_2$ absorption spectra in the *in vivo* setup (Fig. 1b). Fig. 1c presents a representative cross-sectional PA image of a rat brain. The outlines for the brain and motor cortex were drawn based on the rat brain atlas [24] (Fig. 1c). We conducted the *in vivo* experiments according to the protocol shown in Fig. 1d, with a design composed of seizure, control, and negative control groups. Seizure was not induced in the control group subject to VSD + Lexiscan administration. The negative control group served mainly to monitor the hemodynamic change induced by Lexiscan injection and seizure induction without VSD administration.

**Fluorescence quenching-based near-infrared voltage-sensitive dye.** Several cyanine VSDs have been proposed as markers for real-time electrical signal detection [25], and applied for optical imaging of the mitochondrial membrane potential in tumors [26] and fluorescence tracking of electrical signal propagation on a heart. [27] Recently we presented the mechanism of action of a cyanine VSD on the lipid vesicle model.[28] The discussed mechanism of VSD proposes a suppressive PA contrast when neuronal depolarization occurs, while yielding an enhanced contrast for fluorescence. In the present proof-of-principle study, we used the fluorescence quenching-based near-infrared cyanine VSD, IR780 perchlorate (576409, Sigma-Aldrich Co. LLC, MO, United States) with the analogous chemical structure of PAVSD800-2 in our previous study.[28] This VSD yields fluorescence emission leading to a reciprocal PA contrast with non-radiative relaxation of absorbed energy.

**Lipid vesicle phantom preparation for VSD validation.** The lipid vesicle model was prepared using the same procedure as in Zhang et al [28]; 25-mg soybean phosphatidyl-choline (type II) suspended in 1 mL of K+ buffer was used as the lipid vesicles. This vesicle contains 100 mM $K_2SO_4$ and 20 mM HEPES. The suspension was vortexed for 10 min, and followed by 60 min of sonication within bath-type sonicator to yield a translucent vesicle suspension. A $Na^+$ buffer was also prepared, containing100 mM $Na_2SO_4$ and 20 mM HEPES. Afterwards, approximately a 100∶1 $K^+$ gradient across vesicle membrane was established with 10 μL of lipid vesicle suspension added to 1 mL of $Na^+$ buffer. In the vesicle phantom prepared, negative membrane potential (polarized state) was mimicked by adding 2.5 μL of 10 μM valinomycin—a $K^+$ specific ionophore, thereby $K^+$ ions were transported from inside to outside of vesicle membranes. Otherwise, 2.5 μL of 1 mM gramicidin, a nonspecific monovalent cation ionophore, enables $Na^+$ cations to move from outside to inside of vesicle membranes to short circuit the membrane potential (depolarized state). From these controls, our near-infrared VSD positively charged can move in and out through the vesicle membrane, leading to the change in fluorescence quenching depending on their aggregation status. We further investigated the voltage-dependent VSD responses with various levels of membrane potential in lipid vesicle model. We changed the fraction of $K^+$ gradient in the range of 25:1, 50:1, and 100:1 by adding the potassium sulfate in the lipid vesicle suspension (i.e., 2.5 μL, 5 μL, and 10 μL, respectively), while maintaining the Na+ buffer. We expected the logarithmic change in membrane potential levels to the upper

estimation at 100-fold K+ gradient (i.e., -83 mV, -102mV, and -120 mV based on the Nernst equation [28,29]). This will yield a corresponding suppressive PA intensity change.

**Estimation of quantum yield change of VSD.** The quantum yields of the near-infrared VSD in depolarized states ($\Phi'_F$) were estimated based on the equations in our previous literature (Eqs. 8 and 9).[28] The ratio of absorbance and fluorescence emission in depolarized states ($C_{abs}$ and $C_F$) were used compared to those in polarized states, and the estimated fractional changes of PA intensity were calculated for test quantum yields varying from 0 to 0.4 with 0.01 intervals. From the results, the optimal $\Phi'_F$ was chosen, for which the fractional change of PA intensity obtained in lipid vesicle phantom study was presented. The quantum yield in the polarized state ($\Phi_F$) was also estimated by compensating for the absorbance and fluorescence emission changes when depolarized: $\Phi_F=(C_F/C_{abs})\ \Phi'_F$.

**Animal preparation.** For the proposed *in vivo* experiments. 8-9-week-old male Sprague Dawley rats weighing 275-390g were used (Charles Rivers Laboratory, Inc., MA, United States). The use of animals for the proposed experimental protocol was approved by the Institutional Research Board Committee of Johns Hopkins Medical Institute (RA16M225). All animals were anesthetized by intraperitoneal injection with a ketamine (100mg/ml) / xylazine (20 mg/ml) cocktail. (3:1 ratio based on body weight at 1ml/kg). The hair was shaved from the scalp of each rat for improved optical/acoustic coupling for transcranial PA recording. The head of the anesthetized rat was fixed to a stable

position using a standard stereotaxic device. This fixation procedure was required to prevent any unpredictable movement during PA recording of neural activities.

**Chemoconvulsant seizure induction.** Penetylenetetrazole (PTZ), a gamma-aminobutyric acid (GABA) A receptor antagonist was used to induce acute seizures in the animals.[30] PTZ suppresses the inhibitory effects of GABA, thus leading to generation of synchronized depolarizations of neurons in form of epileptiform discharges and seizures. [31-33] To induce global episodic acute seizures in rat brain, an intraperitoneal (IP) injection of PTZ (45 mg/ml) was utilized based on the animal's body weight in a volume of 1ml/kg. Subsequent doses were given if no acute motor seizure was observed in 5-10 minutes after the first PTZ injection. Generally, 1-2 doses were sufficient to induce the motor seizures in our experiments.

**Pharmacological treatment for VSD delivery into blood-brain-barrier.** The lumen of the brain microvasculature consists of brain endothelial cells, and the blood-brain barrier (BBB) is comprised of their tight junctions to control the chemical exchange between neural cells and cerebral nervous system (CNS). In this study, the penetration through BBB were achieved with a pharmacological method using FDA-approved regadenoson (Lexiscan, Astellas Pharma US, Inc. IL, United States). This modulates the Adenosine receptor signaling at BBB layer. [34] For our preliminary studies, the dosage and IV administration method indicated by the manufacturer was utilized. A volume of 150µl of the standard concentration of 0.08 mg/1ml was given to each animal regardless of the weight, followed by 150µl flush of 0.9% sodium chloride for injection. VSD penetration

was expected during the Lexiscan's biological half-life, i.e., 2-4 minutes, thereby the experimental protocol was designed based on the pharmacological assumption. The efficiency of the pharmacological BBB opening was evaluated by PA intensity measurement in the brain tissue region and the frozen-section histopathological analysis with near-infrared fluorescence microscopy. Three different groups were compared: (1) Negative control: VSD-, Lexiscan-; (2) Control: VSD+, Lexiscan; (3) BBB opening: VSD+, Lexiscan+.

***In vivo* experimental protocol.** The *in vivo* protocols were respectively designed for three experimental groups: negative control, control, and seizure groups. Fig. 1d shows the detailed protocol for each group to present the response to the administration of IR780, Lexiscan, and PTZ. Note that each data acquisition was performed for 10 min to cover the biological half-life of Lexiscan (2-3 min). Each dosing protocol of Lexiscan and VSD was as follows: through the jugular vein catheter port located in the neck, 150 µl of Lexiscan 0.4mg/5ml concentration was injected, and 300 µl of VSD was subsequently administrated at 0.1mg/ml concentration, followed by 150 µl of saline solution flush. The control ($N$ = 3) and seizure groups ($N$ = 4) were designed to distinguish the chemoconvulsant effects on neural activity: both groups received IR780 and Lexiscan, but only seizure group had intraperitoneal (IP) injection of PTZ (45mg/ml/kg). The induction of seizure was confirmed by monitoring motor seizure, and another dose of PTZ was injected intraperitoneally when no motor seizure was observed in 5-10 min. In particular, the success of the rat seizure model was determined by the behavioral observation to identify the tonic-clonic movements in whisker, fore and hind-limbs of the

anesthetized rat (Video 4). The behavioral seizure activity was persistently appeared in entire time domain (0 – 10 min) of all the data set included in this paper. The negative control group (*N* = 2) was designed to validate the inability of Lexiscan and PTZ to generate any bias on PA neural activity detection by excluding VSD administration. In the negative control group, first data acquisition was conducted with the Lexiscan dosage, and the second data set was obtained during the chemoconvulsant seizure with Lexiscan dosage.

**Criteria for selecting region-of-interest.** The regions-of-interest (ROI) were selected from left and right motor cortices in a PA image. In PA image, the signals from SSS and SCV would be higher than those in brain tissue region – Brain tissue region naturally contains less blood quantity than those at SSS and SCV since the blood supply is performed by capillaries, not any large vasculatures. Therefore, we used our criteria to select regions-of-interest which can neglect the influence of blood signal at SSS and SCV into cortical regions: (1) The minimal size of the ROIs on each hemisphere was set to 1.86 x 1.54 $mm^2$ within the motor cortex region whose overall dimension is approximately 3 x 2.5 $mm^2$ based on the anatomy of the rat brain atlas shown in Fig. 1c.[24] (2) The positions of ROIs were at least 2.75 mm below the scalp surface to avoid the regions of several other layers covering a brain, i.e., periosteum, skull, dura mater, arachnoid, subarachnoid space, and *pia mater*.[35] The distance is much farther than the axial spatial resolution given by ultrasound transducer (i.e., 479.5 μm of mean FWHM at the depth-of-interest, Fig. 3), thereby the VSD sensing at brain cortical regions could be conducted without any interferences from the superficial dominant clutter regions of

SSS and SCV. (3) Skin surface information may not be sufficient to decide the ROI positions as the melanin contents, a major absorber in scalp, has decreasing absorbance as the wavelength become longer [36]; The 790-nm wavelength used have only around 24% of extinction coefficient compared to those frequently used by other groups for brain imaging all at visible light range (e.g., 500 nm and 570 nm [22], 532 nm [37], 488 nm and 530 nm [21]). Therefore, we are also considering the relative distance from the superior sagittal sinus for ROI positioning. The relative location of SSS and brain tissue involves four layers with different thicknesses. The SSS is in the middle of dura mater (300 μm) which is on top of the arachnoid (75 μm), subarachnoid space (750 μm), and pia mater (75 μm) layers covering a brain. [35] Therefore, the expectable thickness between SSS and brain is 1,050 μm, and motor cortex is extended down to 3-4 mm from the brain tissue surface (bregma 2.2 – 3.2 mm, interaural 11.2 – 12.2 mm [38]). From this justification, the substantial overlap between our ROIs and motor cortex could be ensured since our ROIs are also posed at 2 - 4 mm below the SSS location (Fig. 5).

**Normalized time-frequency analysis.** The real-time video of suppressive PA variation on motor cortex was reconstructed by expanding the ROI to cover the entire brain tissue region, and computing the localized short-time Fourier transform (STFT) spectrogram for its segments (5 x 5 pixels, 18.6 x 19.3 $\mu m^2$ in dimension). The size of a pixel segment would be the actual spatial resolution in our normalized time-frequency analysis for detecting electrophysiological change in neural activity. The individual temporal frequency components of the STFT spectrograms were projected in the

frequency domain to indicate the total amount of suppressive PA variation. To analyze this non-stationary PA intensity series in the time domain, the temporal analysis window was selected with 2-sec of time duration (40 samples) at the 0.5-sec interval, which enables the temporal frequency analysis up to 2Hz with the refreshing rate at 4Hz. Fig. 2 demonstrates the flow chart of our normalized time-frequency analysis to reconstruct the each STFT spectrogram representing PA fluctuation at different frequency. The processing consists of 4 steps for each segment as following:

1. **Step 1:** short-time Fourier transform of a segment;
2. **Step 2:** frequency normalization by the baseband intensity $f_0$ (i.e., 0.1 Hz): $PA(\underline{t}, f) = PA(t, f) / PA(t, f_0)$, where $PA(t, f)$ and $PA(\underline{t}, f)$ are the PA sequence before and after temporal normalization;
3. **Step 3:** linear weighting of each temporal frequency component (i.e., 0.05 to 1 at 0.05 interval for 0 to 2 Hz temporal frequency component at 0.1Hz interval);
4. **Step 4:** temporal normalization to obtain $PA(\underline{t}, \underline{f}) = |PA(\underline{t}, f)/PA(\underline{t}, f_0)|$, in which the $PA_0(\underline{t}, f)$ was the averaged intensity during first 1 min after the VSD injection at each frequency component, $f$;
5. **Step 5:** Construction of the dynamic neural activity maps by allocating the averaged value of $PA(\underline{t}, \underline{f})$ in the frequency dimension at each time point.

Note that the frequency normalization at each pixel segment (Step 2) conduct the crucial role in the analysis; it rejects the global signal fluctuations caused by the variations in laser energy and cerebral blood volume. Also, time-domain normalization (Step 4) and linear weighting of each frequency component (Step 2) reflected the

assumption that PA intensity fluctuating at higher frequency component indicates more vigorous VSD responses evoked by local neural activity, while signal component at lower frequency represent the consistent PA signal from blood context plus stationary VSD response in polarized state. Therefore, this procedure yields higher contrast resolution on VSD response between polarized and depolarized states. The colormap for neural activity map present only suppressive PA intensity change based on the proposed VSD mechanism. [28] To derive the neural activity index of each rat, 20 measurements for each rat have employed by dividing the temporal sequences of PA($\underline{t}$, $\underline{f}$) in every 1 min duration (240 frames) for left/right motor cortexes to calculate the mean values and their standard variations.

**Imaging performance characterization.** The performance of the PA imaging system was evaluated with a phantom experiment. The wire target with 150-μm diameter was placed in the water tank, and the PA data were obtained at 20-, 25-, and 30-mm distance. The depth points include the depth-of-interest in our *in vivo* experiments: the depth of cortical region from the rat scalp surface (~3 – 8 mm) plus the distance between PA probe and rat head surface (i.e., 20 mm). The data recording was also extended for 10 min to validate the expectable range of pulse-to-pulse laser energy fluctuation as well as its long-term variation during *in vivo* experiments. The confidence level of *in vivo* transcranial VSD sensing was also characterized; The normalized contrast-to-noise ratio (CNR) over depth was calculated to quantify the confident level of transcranial VSD sensing *in vivo*. The normalized CNR is given by

$$\overline{CNR}(z) = \frac{1}{S_{SSS}} \max_{x} \frac{\left| S_{signal}(x,z) - S_{noise}(x,z) \right|}{\sigma_{noise}(x,z)}, \quad (1)$$

where ($x$, $z$) is the lateral and axial Cartesian coordinates in the PA image; $S_{SSS}$ is the PA intensity at SSS ($x$ = 0; $z$ = 0); $z$ is the depth index below SSS region in mm scale; $S_{signal}(z)$ is the PA intensity measured from the rat brain image; $S_{noise}(z)$ is the PA intensity measured from the noise image without any absorber in the identical field-of-view size (in the water-filled tank); and $\sigma_{noise}(z)$ is the standard deviation measured from the noise image at each depth index. The maximal CNR values was projected in lateral direction with 10-mm width centered at SSS (e.g., blue dotted box in Fig. 3d). The photo-bleaching *in vivo* was also evaluated. From the ROIs selected at motor cortex region (e.g., white dotted boxes in Fig. 3d), the PA intensity was sequentially measured over time, and normalized with the base intensity at the time range from 0 min to 1 min. Note that the control group ($N$ = 3) was used for these investigations on CNR over the depth-of-interest and photo-bleaching over time.

**EEG validation of neural seizure activity.** To obtain the EEG records of electrical spike discharges that originated from motor cortex, sub-dermal scalp EEG recording electrodes were located at the corresponding locations on motor cortex (Xs in Fig. 9a), the schematic of the rat cranium (three electrodes, 1 recording and 1 reference over motor cortex, 1 ground electrode over rostrum). The EEG signal at motor cortex was recorded with the identical preparation procedures in PA imaging including animal preparation, administration of IR780, Lexiscan, and PTZ, time duration for recording, and interval between sequences in the protocol. Data acquisition was done using

Sirenia software (Pinnacle Technologies Inc., Kansas, USA) with synchronous video capture. Briefly, the data acquisition and conditioning system had a 14-bit resolution, sampling rates of 400 Hz, high pass filters of 0.5 Hz and low pass filters of 60 Hz. The files were stored in .EDF format and scored manually for protocol stages using real time annotations added to the recording during the experiments. EEG power for 10 sec epoch displays within the scoring software package was done using an automated module in Sirenia. Further details of our proposed EEG data acquisition and analysis used in this study are as presented in previous studies.[39,40]

**Validation of protocol for using sub-dermal EEG electrodes to determine toxic CNS effects of VSDs.** VSDs effect on EEG signal from sub-dermal scalp electrodes was investigated in a pilot by direct cortical applications of increasing concentrations of VSDs in anesthetized rat with limited craniotomies while recording synchronous vEEGs (Fig 9a). Increasing concentrations of VSD were tested in the same rat at temporally spaced time-points. Rats were anesthetized with IP injection to ketamine/xylazine and a cranial window made over the right motor cortex. After recording a baseline EEG in the rat for 10-min duration with the craniotomy, the follow-on EEG recording continued to record EEG following application of increasing concentrations of vehicle alone and VSD + vehicle for the same duration of EEG recordings (i.e.; 10 min) allowing comparisons of EEG responses to each increasing gradient of VSD on cortical activity as compared to baseline EEG signature in the same rat.

## Results

Fig. 3 presents the system characterization employed for our neural activity monitoring. We first measured the lateral and axial resolutions from a wire target (Fig. 3a); The FWHMs were the 473.0 µm, 477.8 µm, and 482.6 µm (479.5 ± 2.7 µm in average) in axial direction, and 448.5 µm, 467.6 µm, and 496.2 µm (470.8 ± 24.0 µm in average) in lateral direction at 20 mm, 25 mm, and 30 mm depths, respectively. We also evaluate the short- and long-term laser energy variation; Fig. 3b shows the energy fluctuation when various number of frame averaging is applied: 1, 5, 10, 20, 40 frames. The result proves that the median values were well converged to baseline: 0.10 %, -0.07 %, 0.06 %, 0.14 %, and 0.10 % of fractional change from the global mean value, respectively. Also, the lower and upper adjacent values were limited well with more frame averaging: -8.69 – 8.69, -5.17 – 5.13, -4.52 – 4.86, -3.30 – 4.34, and 2.01 – 3.02 for 1-, 5-, 10-, 20-, 40-frame averaging, respectively. Note that our normalized time frequency analysis employed 40-frame averaging, which would enable to discern the VSD response over about 3 % of instantaneous fractional contrast change from those of laser energy fluctuation which appears consistently over time. In long-term observation for 10 min (Fig. 3c), the fractional PA intensity change was only 0.15 % from the first two minutes to last two minutes (0-2 min: 0.00 ± 1.27 % vs. 8-10 min: 0.15 ± 1.33 %), which have obviously negligible effect in our neural activity recording. Fig. 3d shows the normalized CNR below the depth of SSS as a metric of confidence level in transcranial measurement proposed. The analysis provides positive CNR value (> 0) down to 5 mm depth from the SSS position. This is sufficient imaging depth since the brain surface starts from 1 mm depth from the SSS position, and 4-mm of brain tissue region can be imaged with the imaging system used. We also evaluated the photo-bleaching over time

with the given energy density (i.e., 3.5 mJ/cm$^2$). Fig. 3e present the normalized PA intensity over time at our ROI for neural activity detection. Note that the control group was used for this investigation (*N* = 3). No significant decrease in PA intensity was found at cortical region with the given energy density.

Fig. 4 presents our *in vitro* experimental results using a lipid vesicle model in various $K^+$ gradient levels; From the spectro-photometric / -fluorometric measurements (Fig. 4b), the fractional change in fluorescence emission of the depolarized state over the polarized state were 19.70 %, 61.63 %, and 69.69 % in 25-, 50-, and 100-fold $K^+$ gradient levels (upper estimation limits at -83 mV, -102 mV, and -120 mV of membrane potential, respectively), while preserving a comparable level of absorbance (i.e., fractional absorbance change: 0.07 %, 0.70 %, and 0.21 %, respectively). The PA intensity change presented the corresponding suppressive contrast in depolarized state from a polarized state: -4.91 ± 4.00 %, -11.49 ± 2.00 %, and -14.68 ± 1.41 % in 25-, 50-, and 100-fold $K^+$ gradient levels ($p < 0.005$). From the upper estimation in membrane potential with 100-fold K+ gradient (i.e., 120 mV), the maximal contrast in PA imaging is ~12.24 ± 1.18 % / 100 mV. The quantum yield changes according to the given K+ gradient levels were also estimated based on the theoretical model in our previous literature. [28] The median value in the estimated quantum yield range for each K+ gradient level presents a proportionally-increasing trend as depolarized. Note that the non-specific quantum yield at 25-fold K+ gradient is due to a limited sensitivity to differentiate the subtle membrane potential variation – The specificity of the estimation becomes proportionally improved as more K+ gradient is given.

With the confirmation from the *in vitro* lipid vesicle model, we conducted the *in vivo* validation for transcranial sensing of electrophysiological neural activity in the rat brain according to the protocol shown in Fig. 1d. The PA probe was located on the cross-section at around the Interaural 11.2 mm, Bregma 2.2 mm to monitor the PA signal change originating from motor cortex (Fig. 1c) [24], in eight-to-nine-week-old female Sprague Dawley rats anesthetized with ketamine/xylazine. A rat head was stably fixed with stereotaxic equipment, and was shaved for better acoustic/optic coupling. Videos 1, 2, and 3 present the representative temporal PA image sequence obtained during 9 to 10 min from the seizure, control, and negative control groups. To extract the seizure-induced neural activity from the PA image sequence, we used the short-time Fourier transform (STFT)-based normalized time-frequency analysis method illustrated in Fig. 2. Fig. 5a presents the representative neural activity maps projected in the temporal direction for 10 min in the seizure, control, and negative control groups. The chemoconvulsant seizures induced substantial VSD responses in both motor cortices, while control and negative control groups had consistent records throughout the baseline and comparison phases. The dynamic evolutions of neural activity map over time are presented in Videos 5, 6, and 7. In the respective STFT spectrograms obtained from the regions-of-interest (ROIs) indicated by asterisks in Fig. 5a, significant differences between seizure and control groups were also recorded (Fig. 5b). Fig. 5c shows the fractional change of the neural activity index measured from motor cortexes of each experimental group. The seizure group depicted as much as 140-% more neural activity compared to the baseline: 139.80 ± 42.37 % vs. 0.00 ± 19.99 % ($P < 0.0001$). Otherwise, the control group indicated consistent fractional neural activity indices

compared to those in the baseline phases: 0.00 ± 20.40 % vs. -7.18 ± 25.39 % for baseline and control phases. The negative control group also demonstrated no significance regardless of Lexiscan and PTZ administrations: 0.00 ± 24.71 %, -7.56 ± 23.02 %, 1.30 ± 25.98 % for the cases of Lexiscan-/PTZ-, Lexiscan+/PTZ-, and Lexiscan+/PTZ+, respectively.

We evaluated the efficiency of pharmacological treatment for adenosine receptor signaling modulation by monitoring the evolution of the PA intensity over time with the intravenous injection of ragadenoson (Fig. 6a). The fractional increases from the natural condition (VSD-, Lexiscan-) present statistically significant changes between groups with VSD only and VSD + Lexiscan: 8.64 ± 0.09 % and 13.73 ± 0.09 %, respectively ($P<0.0001$ with 480-time points equal to 2-min range) that indicates the more VSD penetration into the blood-brain barrier (BBB) when using Lexiscan. This contrast enhancement was confirmed by the histopathological analysis on the harvested rat brains (Fig. 6b): (1) negative control group, VSD-, Lexiscan-; (2) control group, VSD+, Lexiscan-; and (3) BBB opening group, VSD+, Lexiscan+. The substantially-enhanced VSD uptake have been identified on the BBB opening group compared to that shown in the control group. On the other hand, negative control group did not present any distinguishable fluorescence contrast. These results present the feasibility of BBB opening based on adenosine receptor signaling modulation using Lexiscan.

We validated the chemoconvulsant-induced seizure activity in the *in vivo* protocol with EEG recording. Using a well-established model of chemoconvulsant-induced *status epilepticus*, we replicated the classic evolution of chemoconvulsant-induced *status epilepticus* using PTZ (Fig. 7). [30] These evolutions as related to bursts of synchronized

neural activity *in vivo* were assessed in two similar experimental protocols mirrored for the EEG and PA experiments. We recorded vEEGs of seizure inductions using PTZ (45mg/kg IP injections) in anesthetized rats. EEG baseline recording continued until a stable seizure induction profile (i.e., continuous burst discharges indicating synchronized neuronal depolarization-related action potentials) was recorded using sub-dermal EEG scalp electrodes. The seizure activity in EEG was associated with tonic-clonic movements in the fore- and hind-limbs of the anesthetized rats, indicating motor cortex involvement (Video 4) recorded on synchronous video during EEG acquisition. The PTZ evolution of status on EEG did not alter with IV VSD treatment.

## Discussion

Here, we present a transcranial PA recording of electrophysiological neural activity *in vivo* using near-infrared VSD for chemoconvulsant seizure in rat brain. In the lipid vesicle phantom experiment, the near-infrared VSD, IR780, clearly revealed the signature of the VSD mechanism in polarization/depolarization events induced by valinomycin and gramicidin (Fig. 4). Based on the validated VSD, the *in vivo* validation study demonstrated that the global seizure activity of the motor cortex was clearly differentiated from the activities of the control and negative control groups (Fig. 5, Video 5, 6, 7). The pharmacological enhancement of VSD delivery into the cortical region by increased permeability of the BBB was confirmed by the histopathological microscopic validation (Fig. 6). The results also strongly agreed with the electrophysiological activities observed by EEG measurement, with an identical experimental setup and protocol (Fig. 7). Our research is intentionally designed to use a low-frequency clinical

ultrasound imaging transducer (center frequency, $f_c$ = 7.1 MHz), which allows totally non-intrusive imaging without any additional invasive procedures such as scalp removal, skull thinning, or craniotomy usually required for high-frequency imaging [22,38] and does not require any sophisticated hardware configuration for narrower isotropic spatial resolution. [21] These previous methods obliged to remove scalp and skull of rat or to use very small-scale subject (i.e., zebrafish). Also, our cortex-of-interest, the motor cortex, is widely extended at frontal brain region down to 5 mm depth (bregma 4.2 mm to bregma -0.92 mm) and up to 5-mm width at each hemisphere (at bregma 3.2 mm), so the cortical region can be monitored with currently-available spatial resolution and sensing depth (Fig. 3). No photo-bleaching effect was identified at the ROI selected. From this specification, the cortical-scale neural depolarization events evoked by chemoconvulsant seizure could be identified with high contrast resolution.

The potentially confounding factors in the experimental setup and protocol employed need to be carefully considered and eliminated. The change in cerebral blood volume (CBV) during chemoconvulsant seizure can generate fluctuations of PA intensity over time that can be misinterpreted as the suppressive VSD response.[41-43] To address this concern, we adjusted two considerations in the *in vivo* protocol and analysis: (1) we allocated 5-10 min of the time duration for hemodynamic stabilization before collecting the PA data, and (2) normalized the STFT spectrogram in both the frequency and time dimensions. Zhang et al. suggested that the total hemoglobin began to change in the pre-ictal period and remained stable after the initiation of tonic-clonic seizure, and the time length from PTZ injection to seizure onset was ~2 min on average,[44] but it was sufficiently covered by our stabilization period in the *in vivo* protocol. The neural activity

map could be stabilized with respect to the CBV change, because the bias on the STFT spectrogram could be rejected during normalization procedures. The negative control group in our *in vivo* protocol is mainly served to test whether these considerations successfully would work. The PA data obtained without any VSD administration went through an identical analysis method to monitor the chemoconvulsant variation of total hemoglobin concentration and capillary CBV. As shown in Fig. 6a (right column), comparable neural activity was obtained between the baseline and seizure phases in the negative control group, and there was no significant gradual change of hemodynamics over time, demonstrating that the hemodynamic interferences were successfully rejected. Moreover, instantaneous blood flow perturbation due to heart beating would not affect the results, as every individual PA frame was compounded for two seconds that include 11–16 heart cycles of a rat (typically 5.5–8 beats per second).

The stability of stereotaxic fixation against the induced motor seizure was also investigated. The counter-hypothesis of this concern was an abrupt disorientation of rat brain due to motor seizure that will induce instantaneous decorrelation between adjacent PA frames. Also, based on the behavioral observation during seizure (Video 4), we anticipated the decorrelation within a sub-second time scale, if it happened. For these hypotheses, we calculated the cross-correlation maps throughout PA frames obtained for 8 minutes (1920 frames, 240 frames/min). Three different time intervals were tested: 0.25 sec, 0.5 sec and 1 sec, which respectively correspond to 4, 2 and 1 frame intervals. For each interval, the minimal correlation projection (MCP) map was composed by finding the minimal value per pixel in temporal direction of the entire stack (Fig. 8). The PA frames with seizure indicated no significant decorrelation between

adjacent PA frames compared to those obtained without seizure. Therefore, the interference by motor seizure could be rejected as potential cause of artifacts in the results.

Toxic CNS effects of VSD is another factor that can alter brain activity. We tested the protocols described in Fig. 1d with varying VSD concentration in rats as a direct application to the cortex (Fig. 9). Results for VSD IR780 with cortical application with cranial windows used in six male rats yielded reliable and reproducible EEG signatures using 10-min recordings for each concentration of IR780. This protocol identified that IR780 concentrations had no effect in altering the baseline EEG in the same rat, indicating no toxic effect on cortical circuit function. Direct cortical application with 100X IR780 resulted in significant EEG background suppression in 4/6 rats, indicating that the certain concentrations of VSD could alter baseline circuit function in the motor cortex. This EEG suppression was recovered to baseline over the 10-min recording period, indicating that the transient effect from the time of application as the 100X VSD either diluted or cleared out of the focal application zone over the 10-min period.

One might argue the necessity of a cellular patch-clamp experiment for *in vitro* VSD characterization. The VSD redistributes within the tissue between the extracellular space and the cytoplasm of polarized cells as a function of membrane potential. When a population of cells depolarize, the total fluorescence in the tissue is increased and the PA signal is decreased. This is intrinsically a tissue-scale measurement, not a single cell measurement. For this reason, a single cell patch clamp calibration would be inappropriate. Using valinomycin and varying the external $K^+$ could theoretically work on a cell suspension, but in practice this treatment rapidly kills living cells and cause them

to swell and bleb. [45,46] We also found that recent PA neuroimaging researches presented their electrophysiological contrast on HEK-293 cells using KCl administration. [22] Though it enabled an artificial level of membrane potential (i.e., 0 – 100 mV), the employed extracellular KCl concentration was much higher (i.e., 12.7, 61.4, 134.8, and 296.0 mM) than the range reported for neuronal injury and death (~ 50 – 90 mM [45,46]). In addition, we do not have the sensitivity to measure PA signals from single patched neurons due to the limited spatial resolution of the commercially-available linear array transducer used for non-invasive deep brain imaging (Figure 3a). In this regard, we believe that the presented lipid vesicle model is the most reliable methodology to characterize our fluorescence quenching yield-changing VSD distributed in both intracellular and extracellular regions. Furthermore, we have good control of the amplitude of the membrane potential across the vesicle membrane by use of a $K^+$ diffusion potential mediated by the $K^+$-specific ionophore valinomycin and reversed by the non-selective ionophore gramicidin (Figure 4). Also, there have been several lipid models (e.g., monolayers, liposome, vesicles, and planar bilayers) as stable methodologies in physicochemical and biophysical studies to better understand the interaction of exogenous molecules with biological membranes. [47-49]

Here, we demonstrated the first proof-of-concept of transcranial PA sensing of neural activity with near-infrared VSD, using a chemoconvulsant seizure model of the rat brain. We plan a number of follow-up efforts to further advance the concept. For instance, the monitoring of seizure activity involved in the hippocampus would be our next step of experimental validation as the region is usually the strongest source of seizure-related activity. The step-by-step approach is required along with the parallel

efforts to overcome the obvious technical challenges related to the optical and acoustic attenuations. We have been successfully using 3.5mJ/cm$^2$ as the energy density to obtain sufficient sensitivity while not inducing photo-bleaching in our measurements, but the confidence level of our transcranial measurement is extended down to 5 mm depth (Fig. 3d,e) , which is not sufficient for hippocampus imaging (5 - 7 mm depth at bregma -1.88). We will further investigate the optimal energy density to increase the penetration depth. Also, contrast enhancing algorithms such as adaptive beamforming could be the solution for this approach.

In addition, we expect that improved signal processing for extracting neural activity from the ubiquitous blood context will enable better characterization of brain function. The present *in vivo* experiments confirmed the possibility of background suppression, but still have artifacts in the sensing area (Baselines in Fig. 5a). Enhanced signal processing and/or use of multi-spectral wavelengths may allow significantly improved spectral unmixing of electrophysiological activities in the brain, leading to development of novel quantitative metrics for real-time brain characterization. Also, there is an abnormal appearance of seizure activity more on a single-side hemisphere (Fig. 5a), and it arise a question of biological factor on the VSD delivery. In our animal preparation, we are using a jugular vein port for VSD + Lexiscan administration. The injected VSD + Lexiscan directly hits a single hemisphere first and perfused through body to reach out to another hemisphere. We are concerned about varying efficiency of BBB opening by Lexiscan concentration, though the amount of VSD would be eventually be equal for both hemispheres after complete body perfusion. To address to this concern, we will change our VSD administration method to tail-vein IV injection for

the complete systematic VSD delivery, and we will also conduct comprehensive investigation on the pharmacological mechanism of BBB opening by Lexiscan. These results will be also presented in the following papers.

Having isotropic resolution with 2-D PA probe would be also an interesting direction to pursue as follow up to the present work. The use of 2-D PA probe would not only allow real-time volumetric information, but also enable the suppression of off-axis interference. Even though we presented that neural activity can be successfully discerned with current 1-D PA probe, its sensitivity might be affected by off-axis interferences especially from the elevation direction because of the limited acoustic lens focusing at a fixed depth. The neuroimaging using 2-D PA probe would reject those interferences by the advanced electrical beamforming capability in axial, lateral, and elevation directions.

The use of localized, non-invasive neural stimulation will allow us to substantially expand our perspectives in real-time brain response to the external stimuli in a totally non-intrusive way.[50] In particular, we envisage that the glutamate receptor modulation using NMDA and/or direct stimulation on sensory cortex can advance the proposed VSD imaging technology. We have recently obtained promising results in NMDA-evoked cortical activity and physiological neural activity imaging at visual cortex with visible light stimulation. [51] However, these results will be presented in the separated publication as its scope is beyond this publication. On the other hand, the integration with ultrasound neuromodulation may have a huge impact on the neuroscientific and clinical efforts by enabling the breakthrough beyond the passive brain investigation, while allowing additional benefits on non-pharmacological BBB opening.[52,53]

The toxicity and biodegradability of IR780 perchlorate dye is another important issue that deserves further evaluation; Even though there have been no long-term and comprehensive toxicity study, we believe that the metabolic products of IR780 should be very similar to ICG, FDA-approved near-infrared cyanine dye, since its absorptive contrast is basically based on same chromophore. This strongly suggest its biocompatibility of our VSD mechanism. We will prove our hypothesis in our future works.

Furthermore, the neural sensing speed should be further improved. Current PA sensing speed is limited to 4 frames per second to obtain sufficient signal sensitivity in the deep brain cortex region with the current laser excitation scheme (20 Hz of pulse repetition rate, 3.5 mJ/cm$^2$). This speed may limit its applicability in research, as it is well known that resting electrophysiological neural activity ranges up to several tens of Hz (e.g., delta: 1–4 Hz; theta: 4–8 Hz; alpha: 8–13 Hz; beta: 13–30 Hz; gamma: 30–50 Hz).[54] We will attempt to resolve the tradeoff in sensitivity by having ~100 Hz of sensing speed. Successful investigation will substantially increase the capability of the proposed approach for understanding brain function in real-time.

## Disclosures

No conflicts of interest, financial or otherwise, are declared by the authors.

## Acknowledgements

Authors thank Dr. Abhinav K. Jha for proofreading the manuscript and providing helpful comments. Also, authors thank Drs. Diane S. Abou and Daniel L. J. Thorek for providing equipment and facilities for *in vitro* experiments using a lipid vesicle model with helpful comments. Financial support was provided by the NIH Brain Initiative under Grant No. R24MH106083-03 and the NIH National Institute of Biomedical Imaging and Bioengineering under Grant No. R01EB01963.

## References


1. K. J. Friston, “Modalities, Modes, and Models in Functional Neuroimaging,” Science **326**(5951), 399–403, American Association for the Advancement of Science (2009) [doi:10.1126/science.1174521].
2. J. J. Frost, “Molecular imaging of the brain: A historical perspective,” Neuroimaging Clinics of North America **13**(4), 653–658 (2003) [doi:10.1016/S1052-5149(03)00094-7].
3. M. E. Raichle and M. A. Mintun, “Brain work and brain imaging.,” Annu. Rev. Neurosci. **29**(1), 449–476 (2006) [doi:10.1146/annurev.neuro.29.051605.112819].
4. S. Grillner et al., “Worldwide initiatives to advance brain research,” Nat. Neurosci. **19**(9), 1118–1122 (2016) [doi:10.1038/nn.4371].
5. P. E. Roland, C. C. Hilgetag, and G. Deco, “Cortico-cortical communication dynamics.,” Front Syst Neurosci **8**, 19, Frontiers Media SA (2014) [doi:10.3389/fnsys.2014.00019].
6. N. V. Vanitha, “Positron emission tomography in neuroscience research,” ANS **18**(2), 36 (2011) [doi:10.5214/ans.0972.7531.1118202].
7. M. E. Raichle, “Behind the scenes of functional brain imaging: a historical and physiological perspective.,” Proc. Natl. Acad. Sci. U.S.A. **95**(3), 765–772, National Acad Sciences (1998) [doi:10.1073/pnas.95.3.765].
8. N. V. Vanitha, “Positron emission tomography in neuroscience research,” ANS **18**(2), 36 (2011) [doi:10.5214/ans.0972.7531.1118202].
9. N. K. Logothetis, “What we can do and what we cannot do with fMRI - ProQuest,” Nature (2008).
10. M. G. Berman, J. Jonides, and D. E. Nee, “Studying mind and brain with fMRI.,” Social cognitive and affective neuroscience **1**(2), 158–161 (2006) [doi:10.1093/scan/nsl019].
11. E. M. C. Hillman, “Optical brain imaging in vivo: techniques and applications from animal to man.,” J. Biomed. Opt. **12**(5), 051402–051402–28, International Society for Optics and Photonics (2007) [doi:10.1117/1.2789693].
12. A. Devor et al., “Frontiers in optical imaging of cerebral blood flow and metabolism.,” J. Cereb. Blood Flow Metab. **32**(7), 1259–1276, Nature Publishing Group (2012) [doi:10.1038/jcbfm.2011.195].
13. C. Heo et al., “A soft, transparent, freely accessible cranial window for chronic imaging and electrophysiology.,” Sci Rep **6**(1), 27818, Nature Publishing Group (2016) [doi:10.1038/srep27818].
14. G. E. Strangman, Z. Li, and Q. Zhang, “Depth sensitivity and source-detector separations for near infrared spectroscopy based on the Colin27 brain template.,” PLoS ONE **8**(8), X.-N. Zuo, Ed., e66319, Public Library of Science (2013) [doi:10.1371/journal.pone.0066319].
15. A. Torricelli et al., “Time domain functional NIRS imaging for human brain mapping.,” NeuroImage **85 Pt 1**, 28–50 (2014) [doi:10.1016/j.neuroimage.2013.05.106].
16. L. V. Wang and S. Hu, “Photoacoustic tomography: in vivo imaging from organelles to organs.,” Science **335**(6075), 1458–1462 (2012) [doi:10.1126/science.1216210].

17. X. Wang et al., “Noninvasive laser-induced photoacoustic tomography for structural and functional in vivo imaging of the brain,” Nat Biotechnol **21**(7), 803–806, Nature Publishing Group (2003) [doi:10.1038/nbt839].
18. L. Nie et al., “Photoacoustic tomography through a whole adult human skull with a photon recycler,” J. Biomed. Opt. **17**(11), 110506, International Society for Optics and Photonics (2012) [doi:10.1117/1.JBO.17.11.110506].
19. W. Li et al., “In Vivo Photoacoustic Imaging of Brain Injury and Rehabilitation by High-Efficient Near-Infrared Dye Labeled Mesenchymal Stem Cells with Enhanced Brain Barrier Permeability,” Adv. Sci. **34**, 1700277–11 (2017) [doi:10.1002/advs.201700277].
20. Y. Liu et al., “Highly specific noninvasive photoacoustic and positron emission tomography of brain plaque with functionalized croconium dye labeled by a radiotracer,” Chem Sci **8**, 2710–2716, Royal Society of Chemistry (2017) [doi:10.1039/C6SC04798J].
21. X. L. Deán-Ben et al., “Functional optoacoustic neuro-tomography for scalable whole-brain monitoring of calcium indicators,” Light Sci Appl **5**(12), e16201–e16207, Nature Publishing Group (2016) [doi:10.1038/lsa.2016.201].
22. B. Rao et al., “Photoacoustic imaging of voltage responses beyond the optical diffusion limit.,” Sci Rep **7**(1), 2560 (2017) [doi:10.1038/s41598-017-02458-w].
23. “American National Standard for the Safe Use of Lasers.,” Annals of Internal Medicine **82**(1), 132 (1975) [doi:10.7326/0003-4819-82-1-132_2].
24. G. Paxinos and C. Watson, *The Rat Brain in Stereotaxic Coordinates*, Seventh edition, Elsevier Academic Press (2014).
25. J. S. Treger et al., “Real-time imaging of electrical signals with an infrared FDA-approved dye,” Biophysj **107**(6), L09–L012 (2014) [doi:10.1016/j.bpj.2014.07.054].
26. S. Onoe et al., “Investigation of cyanine dyes for in vivo optical imaging of altered mitochondrial membrane potential in tumors.,” Cancer Med **3**(4), 775–786 (2014) [doi:10.1002/cam4.252].
27. I. Martišienė et al., “Voltage-Sensitive Fluorescence of Indocyanine Green in the Heart,” BPJ **110**(3), 723–732, Biophysical Society (2016) [doi:10.1016/j.bpj.2015.12.021].
28. H. K. Zhang et al., “Listening to membrane potential: photoacoustic voltage-sensitive dye recording,” J. Biomed. Opt. **22**(4), 045006 (2017) [doi:10.1117/1.JBO.22.4.045006].
29. M. D. Archer, *Electrochemistry, Past and Present*, in Electrochemistry, Past and Present **390**, J. T. Stoke and M. V. Orna, Eds., pp. 115–126, American Chemical Society, Washington, DC (1989) [doi:10.1021/bk-1989-0390.ch008].
30. W. Löscher, “Animal Models of Seizures and Epilepsy: Past, Present, and Future Role for the Discovery of Antiseizure Drugs.,” Neurochem. Res. **42**(7), 4 ed., 1873–1888 (2017) [doi:10.1007/s11064-017-2222-z].
31. H. F. Bradford, “Glutamate, GABA and epilepsy,” Progress in Neurobiology **47**(6), 477–511 (1995) [doi:10.1016/0301-0082(95)00030-5].
32. T. de Boer, J. C. Stoof, and H. van Duijn, “The effects of convulsant and anticonvulsant drugs on the release of radiolabeled GABA, glutamate,

noradrenaline, serotonin and acetylcholine from rat cortical slices.," Brain Res. **253**(1-2), 153–160 (1982) [doi:10.1016/0006-8993(82)90682-5].
33. P. P. De Deyn and R. L. Macdonald, "Effects of antiepileptic drugs on GABA responses and on reduction of GABA responses by PTZ and DMCM on mouse neurons in cell culture.," Epilepsia **30**(1), 2nd ed., 17–25, Blackwell Publishing Ltd (1989) [doi:10.1111/j.1528-1157.1989.tb05275.x].
34. A. J. Carman et al., "Adenosine receptor signaling modulates permeability of the blood-brain barrier.," Journal of Neuroscience **31**(37), 13272–13280, Society for Neuroscience (2011) [doi:10.1523/JNEUROSCI.3337-11.2011].
35. K. Nowak et al., "Optimizing a Rodent Model of Parkinson's Disease for Exploring the Effects and Mechanisms of Deep Brain Stimulation," Parkinson's Disease **2011**(2754), 1–19 (2011) [doi:10.4061/2011/414682].
36. S. L. Jacques and S. Prahl, *Extinction coefficient of melanin*, OMLC (https://omlc.org/spectra/melanin/extcoeff.html) (2013).
37. J. Yao et al., "High-speed label-free functional photoacoustic microscopy of mouse brain in action," Nat Meth **12**(5), 407–410 (2015) [doi:10.1038/nmeth.3336].
38. G. Paxinos, C. W. N. Y. Academic, 1998, *A stereotaxic atlas of the rat brain*.
39. D. A. Adler et al., "Circadian cycle-dependent EEG biomarkers of pathogenicity in adult mice following prenatal exposure to in utero inflammation.," Neurosci Res **275**, 305–313 (2014) [doi:10.1016/j.neuroscience.2014.06.022].
40. M. V. Johnston et al., "Twenty-four hour quantitative-EEG and in-vivo glutamate biosensor detects activity and circadian rhythm dependent biomarkers of pathogenesis in Mecp2 null mice.," Front Syst Neurosci **8**(JUNE), 118 (2014) [doi:10.3389/fnsys.2014.00118].
41. H. Goldman et al., "Cerebrovascular responses to pentylenetetrazol: time and dose dependent effects," Epilepsy Res. **12**, 227–242 (1992).
42. A. Nehlig et al., "Absence seizures induce a decrease in cerebral blood flow: Human and animal data," J. Cereb. Blood Flow Metab. **16**(1), 147–155 (1996).
43. Y. Hoshi and M. Tamura, "Dynamic changes in cerebral oxygenation in chemically induced seizures in rats: study by near-infrared spectrophotometry.," Brain Res. **603**(2), 215–221 (1993).
44. T. Zhang et al., "Pre-seizure state identified by diffuse optical tomography," Sci Rep **4**(1), 113–10 (2014) [doi:10.1038/srep03798].
45. R. R. Ramnath, K. Strange, and P. A. Rosenberg, "Neuronal injury evoked by depolarizing agents in rat cortical cultures.," Neurosci Res **51**(4), 931–939 (1992).
46. M. Takahashi, S. Y. Liou, and M. Kunihara, "Ca(2+)- and Cl(-)-dependent, NMDA receptor-mediated neuronal death induced by depolarization in rat hippocampal organotypic cultures.," Brain Res. **675**(1-2), 249–256 (1995).
47. V. Rosilio, "How Can Artificial Lipid Models Mimic the Complexity of Molecule–Membrane Interactions?," Advances in Biomembranes and Lipid Self-Assembly, Elsevier (2018).
48. F. Mazur et al., "Liposomes and lipid bilayers in biosensors," Advances in Colloid and Interface Science **249**, 88–99 (2017) [doi:10.1016/j.cis.2017.05.020].

49. W. F. Paxton et al., “Monitoring and modulating ion traffic in hybrid lipid/polymer vesicles,” Colloids and Surfaces B: Biointerfaces **159**, 268–276 (2017) [doi:10.1016/j.colsurfb.2017.07.091].
50. P. M. Lewis et al., “Brain Neuromodulation Techniques: A Review.,” Neuroscientist, 1073858416646707, SAGE Publications (2016) [doi:10.1177/1073858416646707].
51. J. Kang et al., “Transcranial recording of stimulated neuronal activity variation *in vivo* using photoacoustic voltage-sensitive dye imaging,” presented at SPIE BiOS: Biomedical Optics, 31 January 2017, San Fransicso, CA.
52. Y. Tufail et al., “Ultrasonic neuromodulation by brain stimulation with transcranial ultrasound.,” Nat Protoc **6**(9), 1453–1470, Nature Publishing Group (2011) [doi:10.1038/nprot.2011.371].
53. P.-C. Chu et al., “Neuromodulation accompanying focused ultrasound-induced blood-brain barrier opening.,” Sci Rep **5**, 15477 (2015) [doi:10.1038/srep15477].
54. D. Mantini et al., “Electrophysiological signatures of resting state networks in the human brain,” Proc. Natl. Acad. Sci. U.S.A. **104**(32), 13170–13175, National Acad Sciences (2007) [doi:10.1073/pnas.0700668104].

## BIOGRAPHIES

**Jeeun Kang** is currently a postdoctoral fellow in the Laboratory of Computational Sensing and Robotics and the Radiology Department at The Johns Hopkins University. He received Ph.D. degree in Electronic Engineering from Sogang University, South Korea. He was recruited in 2016 to research *in vivo* photoacoustic neuroimaging at the Johns Hopkins University/Hospital. His research interests include advanced multi-modal imaging and therapy based on ultrasound, photoacoustic, and optical modalities for neuroscience and neuro engineering.

**Haichong K. Zhang** is a postdoctoral fellow in the Laboratory of Computational Sensing and Robotics at The Johns Hopkins University. He received a B.S. and a M.S. in Human Health Sciences from Kyoto University, Japan. After completing his master's degree, he joined the Johns Hopkins University, and received a M.S. and a Ph.D. in Computer Science. His research interests include advanced robotic instrumentation and imaging with emphasis on ultrasound and photoacoustics for biomedical applications.

**Shilpa D. Kadam** is Assistant Professor in the Department of Neurology at the Johns Hopkins University School of Medicine and at the Kennedy Krieger Institute. She is Director of the pre-clinical *in-vivo* EEG-core at KKI. Her expertise is in neuroscience using translational models of developmental disabilities and mechanisms underlying epileptogenesis. She is an active task force member of the International League Against Epilepsy and a council member of the Research and Training committee of the American Epilepsy Society.

**Julie Fedorko** received her degree in neuroscience at Pomona College in 2016. Upon graduating, she came to Johns Hopkins to pursue research funded by the White House BRAIN Initiative. Currently, she studies synthetic drugs of abuse at the National Institute on Drug Abuse, and will be attending medical school in the fall.

**Heather Valentine** is an *in vivo* pre-clinical manager in the department of Radiology/Nuclear Medicine at the Johns Hopkins University. She plans, coordinate, supervises and assist with project related animal studies in Dr. Dean Wong's laboratory. She handles all collaborative studies between groups within the University, as well as Industry collaborations. Her expertise is in neuroscience research and translational animal model development.

**Adarsha P. Malla** is a Research Technologist in the Department of Neuroscience at Johns Hopkins University's School of Medicine. Adarsha is a graduate of the B.S. Biomedical Engineering Program at Johns Hopkins University with a focus area of Neuroengineering. His research work spans ultrasound biophysics, photoaucoustic neuromodulation, molecular neuroscience, statistical connectomics, and medical device design and development. He is currently working in the labs of Dr. Solomon H. Snyder and Dr. Emad M. Boctor.

**Ping Yan** received his BSc and MS degrees in chemistry at the University of Science and Technology of China. He completed his PhD degree in Chemistry at the Columbia University. Formerly, he was a postdoc at the University of Connecticut Health Center, now he is an assistant professor at the Berlin Center for Cell Analysis and Modeling. His research focuses on the development of voltage sensitive dyes for optical imaging and photoacoustic imaging.

**Jin U. Kang** is Jacob Suter Jammer Professor of the Department of Electrical and Computer Engineering at the Johns Hopkins University and a member of Kavli Neuroscience Discovery Institute. He is an expert in optical imaging, sensing, fiber optic devices and photonic systems. He is a Program Chair of A&T, CLEO. He is a fellow of the Optical Society of America (OSA), SPIE, and of American Institute for Medical and Biological Engineering (AIMBE).

**Arman Rahmim** is Associate Professor of Radiology and Electrical & Computer Engineering at the Johns Hopkins University. He received his M.Sc. in condensed matter physics and Ph.D in medical imaging physics. He was recruited in 2005 to lead the high-resolution brain PET imaging physics program at the Johns Hopkins University/Hospital, where he continues to conduct research (rahmimlab.com) in tomographic image generation and analysis, including brain, cardiac and oncologic applications.

**Albert Gjedde** is Professor of Translational Neurobiology at the University of Southern Denmark, Emeritus Professor of Neurobiology and Pharmacology at the University of Copenhagen, and Adjunct Professor at both the McGill University, Canada, and Johns Hopkins University, USA. He currently serves on the Program Committee of the Horizon2020 program of the European Commission. He is Fellow of the American Association for the Advancement of Science, the Royal Society of Canada, the American College of Neuropsychopharmacology, the Academy of Europe, and the Norwegian Academy of Science and Letters.

**Leslie M. Loew** is Director of the Berlin Center for Cell Analysis and Modeling and holds the Boehringer Ingelheim Chair in Cell Sciences at the UConn School of Medicine. His research focuses on cellular biophysics. He is known for his widely used voltage sensitive dyes, the development of SHG microscopy, and the Virtual Cell, a computational environment for modeling cell function. He served as Editor in Chief of Biophysical Journal from 2012-2017.

**Dean F. Wong** is Professor of Radiology, Psychiatry, Neurology, and Neuroscience at the Johns Hopkins University. He has 39 years of brain PET research starting with the team first imaging human dopamine D2 neuroreceptors and applications in aging and neuropsychiatric disorders. He has pioneered many preclinical and human neuroreceptor and amyloid/tau radiopharmaceuticals and target engagement of CNS therapies. His ultimate goal is human imaging of functional networks in the millisecond range.

**Emad M. Boctor** is Assistant Professor of Radiology, Computer Science, and Electrical and Computer Engineering at Johns Hopkins University. He is the director of the Medical Ultrasound Imaging and Intervention Collaboration (MUSiiC) research laboratory. His research interest for over 12 years has focused on advanced ultrasound instrumentation and imaging, a subject in which he has over 60 peer-reviewed manuscripts and 150 conference articles, more than 25 pending/issued patents, and more than 10 industry collaborators.

## FIGURE CAPTIONS

**Fig. 1. Transcranial VSD sensing setup using PA imaging system:** (a) schematic diagram of experimental setup; (b) absorbance spectra of VSD, deoxy- and oxy-hemoglobin. Dotted line indicates the wavelength used in *in vivo* experiment, i.e., 790 nm; (c) cross-sectional PA image of cerebral cortex; (d) *in vivo* experimental protocol. SSS: Superior sagittal sinus; SCV: Superior cortical veins. SSS: superior sagittal sinus; SCV: superior cortical veins; L-MC/R-MC: left/right motor cortex. Note that the outlines for brain and motor cortex in Fig. 1c was drawn based on the rat brain atlas (Interaural 11.2 mm, Bregma 2.2 mm) [24] The success of seizure induction was confirmed by tonic-clonic movements in the fore and hind-limbs of the anesthetized rat during the experiments (Video 4, MPEG, 1.8MB).

**Fig. 2. Normalized time-frequency analysis method:** (a) Flow chart of the proposed signal analysis; (b) Frequency-projected neural activity map for entire field-of-view and (c) spatial-projected spectrogram for specific motor cortex region-of-interest. The white bar in Fig. 2b indicates 1 mm. ($X$, $Y$): lateral and axial indices of each pixel segment for the normalized time-frequency analysis; ($x$, $y$): lateral and axial pixel indices in each pixel segment.

**Fig. 3. Characterization of the PA imaging system:** (a) spatial full-width-half-maximum (FWHM) beam profile in axial and lateral directions at various depth-of-interest (i.e., 20, 25, and 30 mm). (b) Fractional change in energy fluctuation with various number of frame averaging (i.e., 1, 5, 10, 20, 40 frames). (c) Long-term comparison in laser energy fluctuation between 0-2 min to 8-10 min time ranges. (d) Normalized contrast-to-noise ratio (CNR) laterally-projected over the depth range below SSS. Blue dotted rectangular in the exemplary image present the region for pixel-by-pixel CNR calculation. White bar on bottom-right indicates 1 mm. (e) Validation data for photo-bleaching at the ROI indicated with white dotted boxes in Fig. 3d.

**Fig. 4. *In vitro* experimental results using lipid vesicle membrane model with VSD.** (a) Lipid vesicle membrane model. (b) Fractional changes of the spectro-photometric / fluorometric measurements in the depolarized state over the polarized state: absorbance and fluorescence emission. (c) Photoacoustic intensity spectrum at 25-, 50-, and 100-fold K+ gradients and fractional changes at 790 nm ($p$ = 0.055, 0.010, and 0.002 between polarized and depolarized states for 25-, 50-, and 100-fold K+ gradients, respectively. (d) The estimated quantum yield change for each K+ gradient level. [28] The median values were presented in the estimated quantum yield range for each K+ gradient level.

**Fig. 5. The representative PA sensing of electrophysiological neural activity:** (a) Exemplary time-averaged neural activity maps: Seizure (Video 5), control (Video 6), and negative control (Video 7); (b) STFT spectrograms of VSD response of each protocol; (c) neural activity index projected over 10 min in entire animals in seizure, control, and negative control groups. Note that the regions-of-interest in the STFT spectrograms are indicated with asterisk marks in the respective neural activity map. The representative temporal evolution of PA intensity over time can be found for seizure (Video 1), control (Video 2), and negative control (Video 3) groups. White bar in Fig. 5a indicates 1 mm. (Video 1-3, 5-7, MPEG, 1.3MB/Video)

**Fig. 6. *In vivo* validation of VSD delivery to a rat brain:** (a) Fractional changes of PA intensity depending on Adenosine receptor signaling modulation using intravenous regadenoson administration. Each PA sequences, i.e., VSD only and VSD + regadenoson, was measured from the brain tissue region (3 mm below the skin surface), and projected during last 2 min (8-10 min, 480 times points). (b) histopathological analysis on negative control (VSD-, Lexiscan-), control (VSD+, Lexiscan-), and BBB opening (VSD+, Lexiscan+) groups.

**Fig. 7. Evolution of EEG signal in the *in vivo* protocol identical to transcranial PA imaging:** (a) Representative EEG tracs recorded from rat motor cortex before and during induction of status epilepticus using chemoconvulsant PTZ. The baseline and control EEG traces represent EEG activity in an anesthetized rat (see methods) with and without IR780+lexiscan given at the dosage found to not alter baseline EEG activity in the pilot study. PTS seizure induction proceeded in classical style described previously wherein episodic epileptiform burst activity evolved into status epilepticus with intermittent occurrence of seizures and stable interictal activity. (b) EEG spectral quantitation of the EEG recording done every 10 sec epoch during the EEG showed the expected progression in EEG power associated with evolution of the PTZ induced status epilepticus. Time line of PTZ injections indicated with arrows. Expanded EEG traces on top show the uniform epileptiform discharges after following second PTZ injection and below a seizure event followed of post-ictal suppression indicating the termination of that event.

**Fig. 8. Minimal correlation projection (MCP) image using cross-correlation coefficients with varying time interval, i.e., 0.25 sec, 0.5 sec, and 1 sec, which respectively corresponds to 1, 2, 4 frame intervals with the imaging rate at 4 frames per second.** (a) region of interest for the inter-frame cross-correlations, (b) MCP images of baseline (PTZ-, VSD-) and seizure groups (PTZ+, VSD-) for brain tissue region. (c) Cross-correlation coefficient for varying time intervals.

**Fig. 9. VSD toxicity study using EEG recordings during direct cortical applications using a cranial window in rats.** (a) Schematic of experimental protocol. A rectangular cranial window drilled under anesthesia overlying unilateral motor cortex. Duramater was kept intact. Following craniotomy, a small window was made in duramater without traversing blood vessels. (b) EEG recording of baseline brain activity under anesthesia was followed by using a hamilton micro syringe to apply increasing concentrations of IR780 directly to the cortical surface via window made in duramater. Base EEG remained unaltered at lower concentrations but showed significant background suppression after applying a 100X solution. This study allowed us to determine the concentration of IR780 10X for all PA experiments. (c) EEG power spectral quantification for every 10-sec epoch of EEG over the duration of the recording confirmed EEG suppression with the 100X dose.

## VIDEO CAPTIONS

**Video 1.** The representative PA sequence: seizure group:

**Video 2.** The representative PA sequence: control group:

**Video 3.** The representative PA sequence: negative control group:

**Video 4.** The tonic-clonic movements in the fore and hind-limbs of the anesthetized rat:

**Video 5.** The representative PA video of neural activity map in seizure group:

**Video 6.** The representative PA video of neural activity map in control group:

**Video 7.** The representative PA video of neural activity map in negative control group:

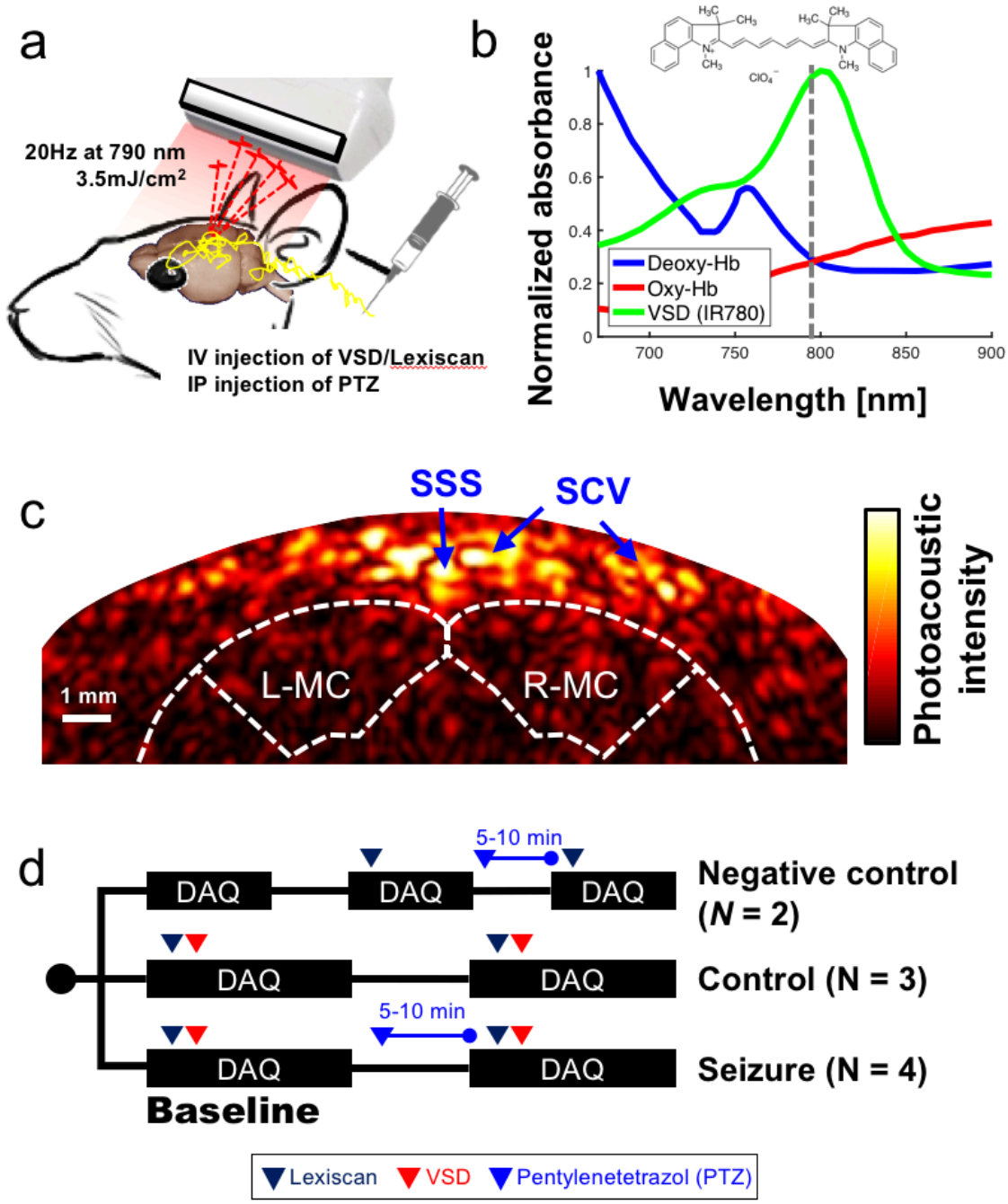
a
20Hz at 790 nm
3.5mJ/cm²
IV injection of VSD/Lexiscan
IP injection of PTZ
b
Normalized absorbance
Wavelength [nm]
Deoxy-Hb
Oxy-Hb
VSD (IR780)
c
SSS
SCV
L-MC
R-MC
1 mm
Photoacoustic intensity
d
5-10 min
DAQ
Negative control (N = 2)
Control (N = 3)
Seizure (N = 4)
Baseline
Lexiscan
VSD
Pentylenetetrazol (PTZ)

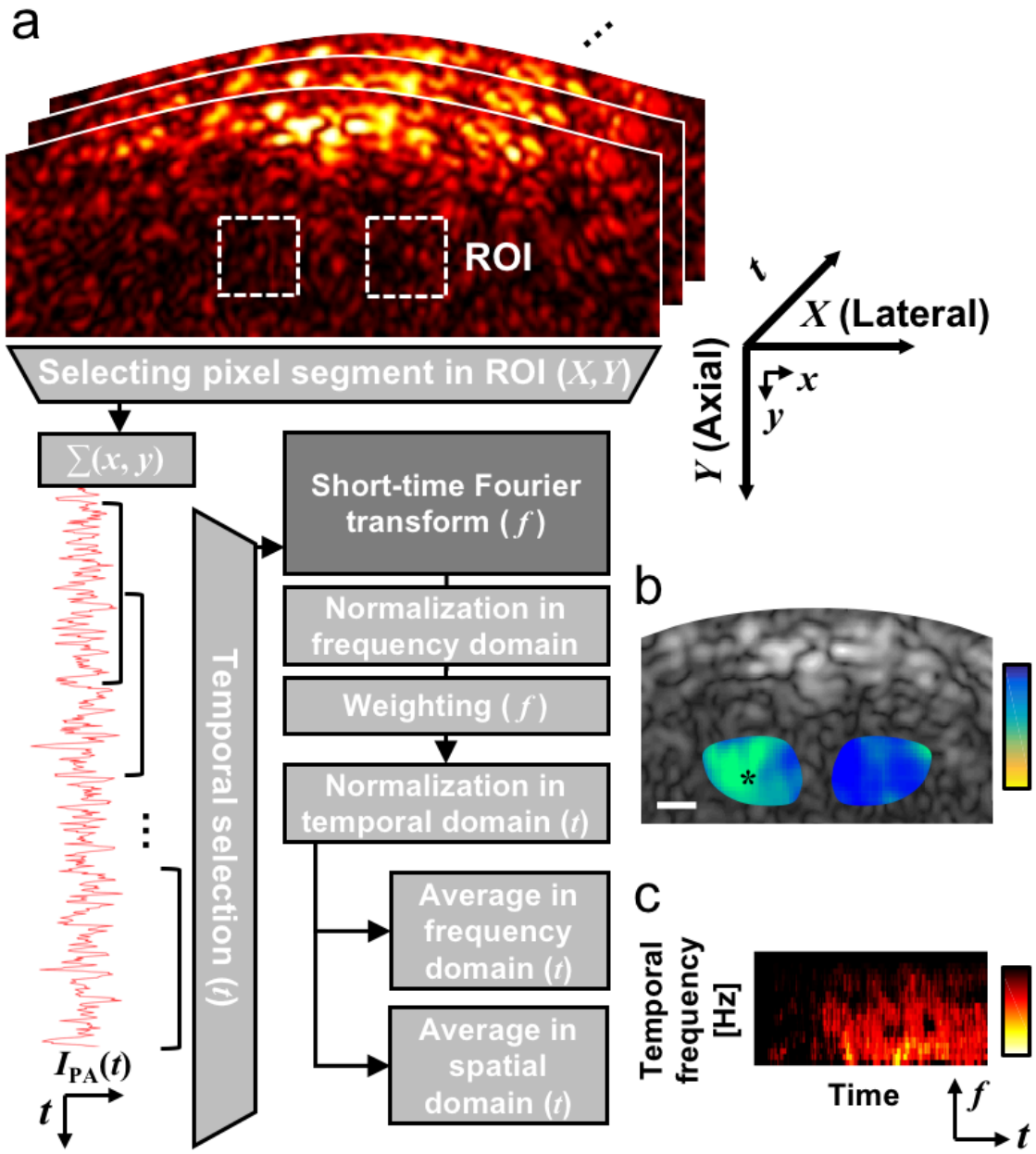
a
ROI
Selecting pixel segment in ROI (X,Y)
∑(x, y)
Temporal selection (t)
Short-time Fourier transform (f)
Normalization in frequency domain
Weighting (f)
Normalization in temporal domain (t)
Average in frequency domain (t)
Average in spatial domain (t)
I_PA(t)
t
X (Lateral)
Y (Axial)
x
y
b
c
Temporal frequency [Hz]
Time
f
t

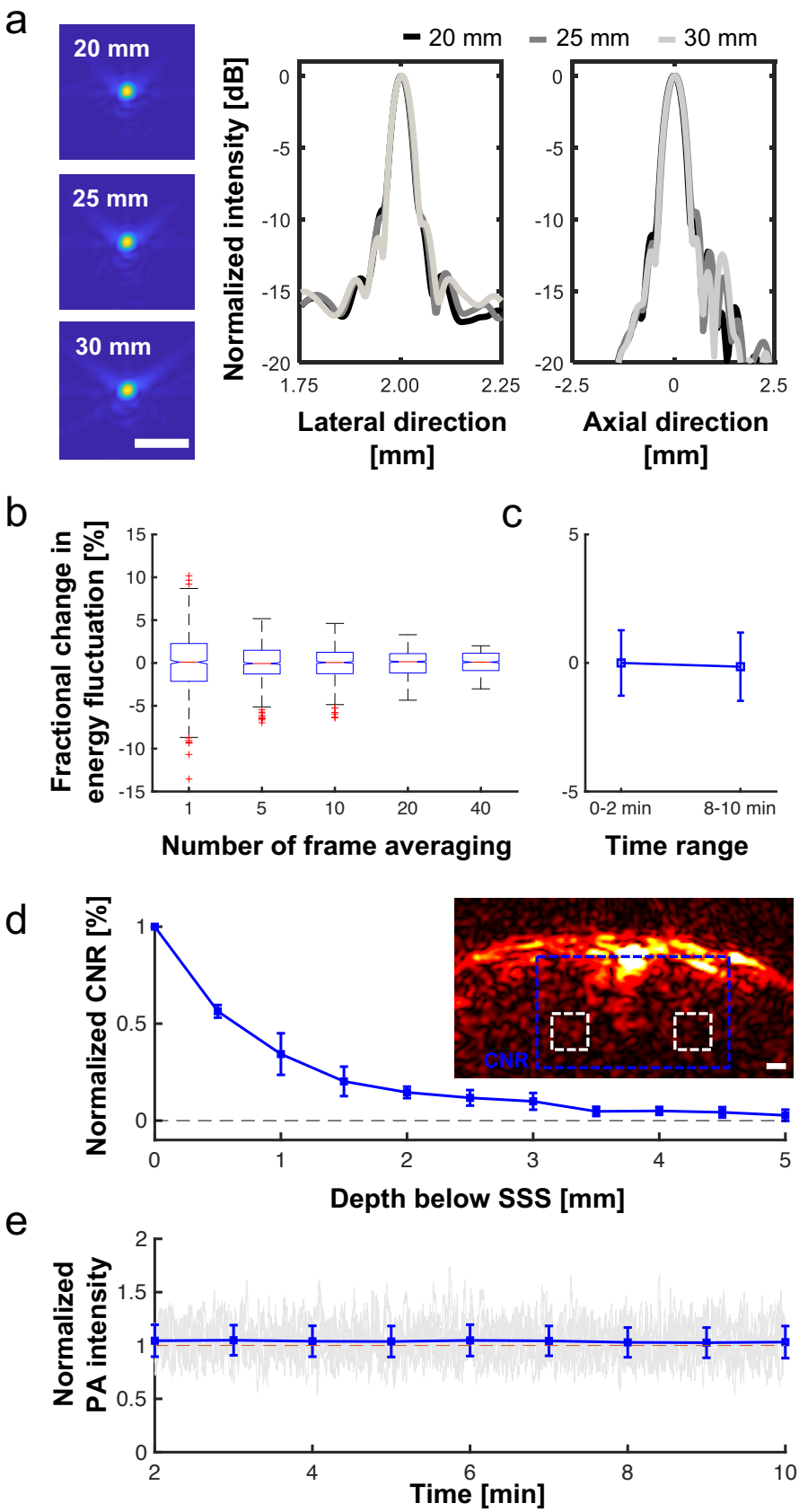
a
20 mm
25 mm
30 mm
20 mm
25 mm
30 mm
Normalized intensity [dB]
Lateral direction [mm]
Axial direction [mm]
b
Fractional change in energy fluctuation [%]
Number of frame averaging
c
0-2 min
8-10 min
Time range
d
Normalized CNR [%]
CNR
Depth below SSS [mm]
e
Normalized PA intensity
Time [min]

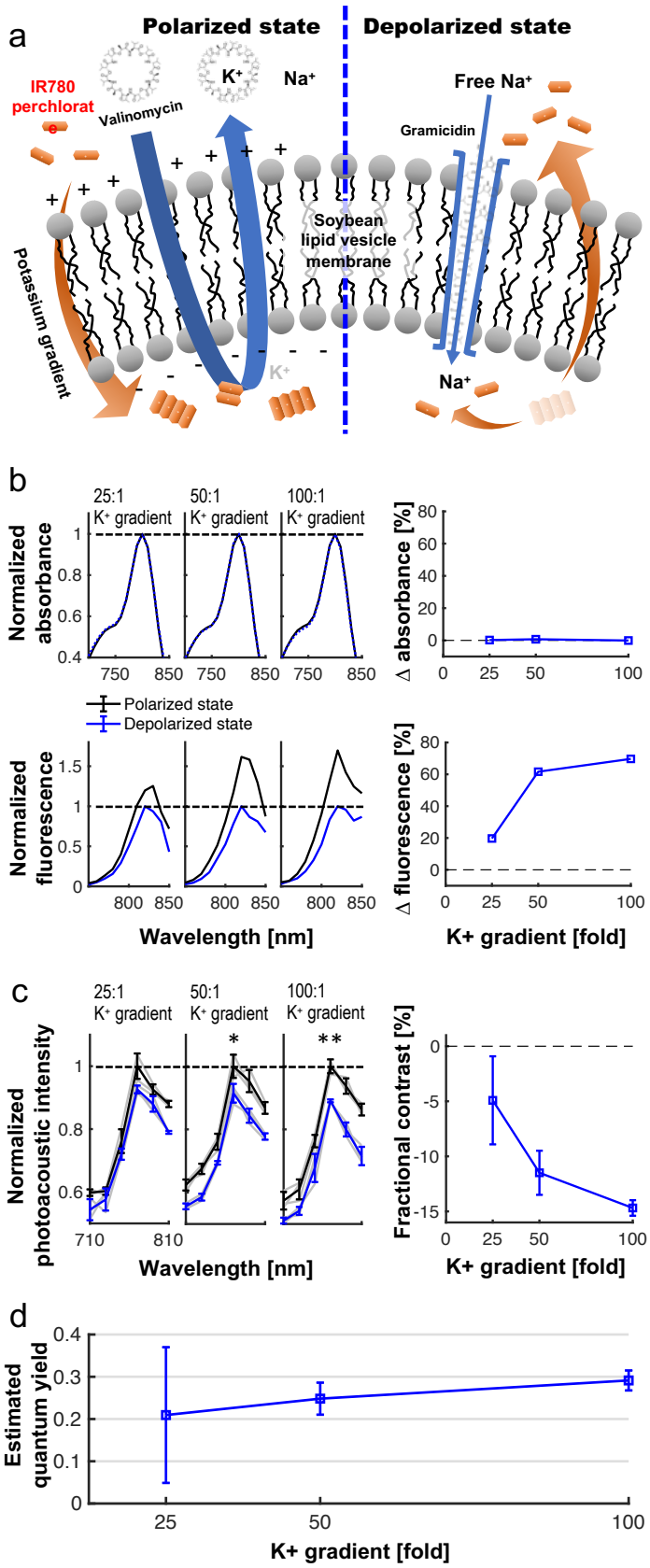
a
Polarized state
Depolarized state
IR780 perchlorate
Valinomycin
K+
Na+
Free Na+
Gramicidin
Soybean lipid vesicle membrane
Potassium gradient
K+
Na+
b
25:1 K+ gradient
50:1 K+ gradient
100:1 K+ gradient
Normalized absorbance
Δ absorbance [%]
Polarized state
Depolarized state
Normalized fluorescence
Δ fluorescence [%]
Wavelength [nm]
K+ gradient [fold]
c
25:1 K+ gradient
50:1 K+ gradient
100:1 K+ gradient
Normalized photoacoustic intensity
Fractional contrast [%]
Wavelength [nm]
K+ gradient [fold]
d
Estimated quantum yield
K+ gradient [fold]

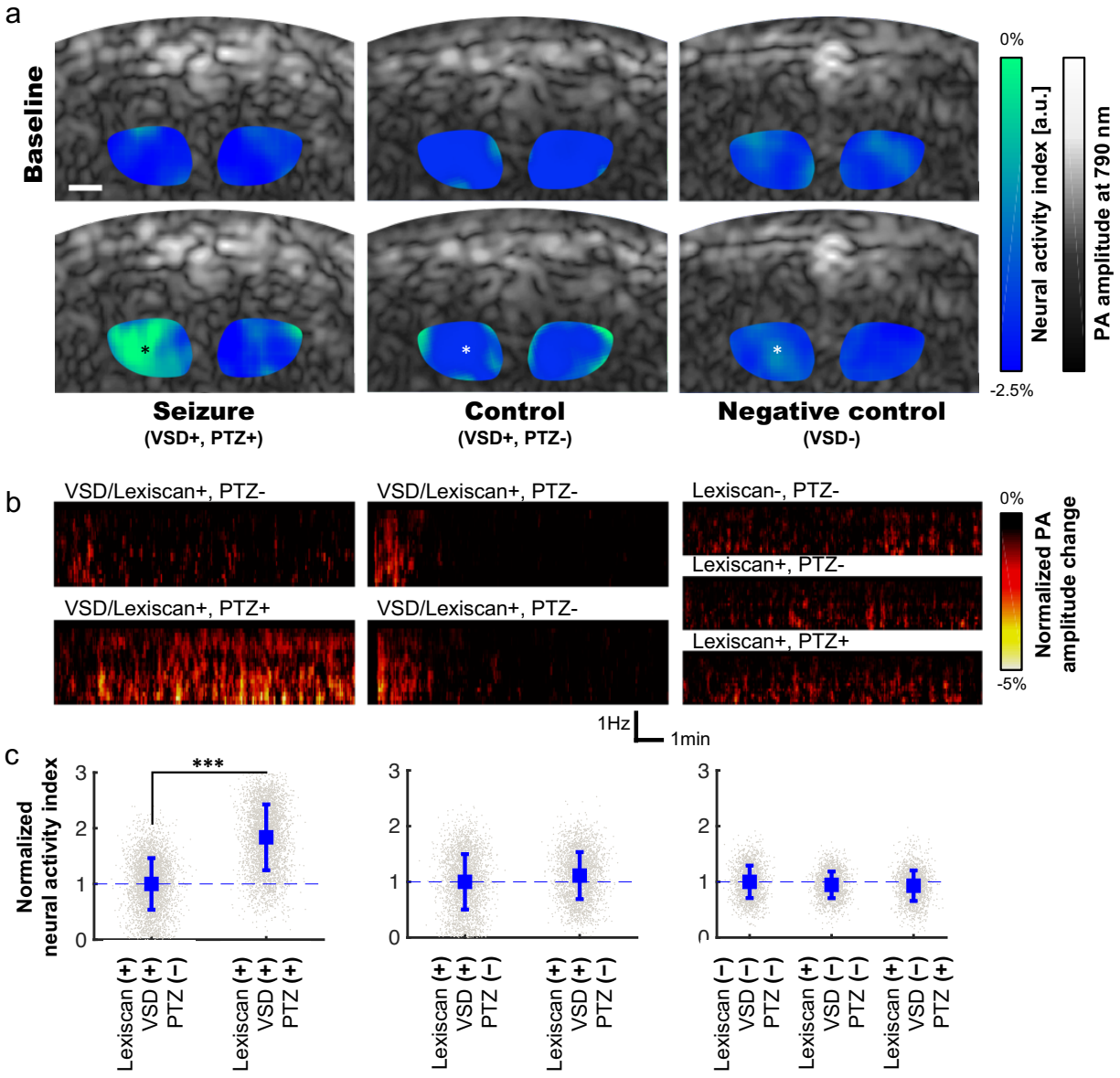
a
Baseline
0%
-2.5%
Neural activity index [a.u.]
PA amplitude at 790 nm
Seizure
(VSD+, PTZ+)
Control
(VSD+, PTZ-)
Negative control
(VSD-)
b
VSD/Lexiscan+, PTZ-
VSD/Lexiscan+, PTZ-
Lexiscan-, PTZ-
Lexiscan+, PTZ-
VSD/Lexiscan+, PTZ+
VSD/Lexiscan+, PTZ-
Lexiscan+, PTZ+
0%
-5%
Normalized PA amplitude change
1Hz
1min
c
Normalized neural activity index
***
Lexiscan (+) VSD (+) PTZ (−)
Lexiscan (+) VSD (+) PTZ (+)
Lexiscan (+) VSD (+) PTZ (−)
Lexiscan (−) VSD (−) PTZ (−)
Lexiscan (+) VSD (−) PTZ (−)
Lexiscan (+) VSD (−) PTZ (+)

a

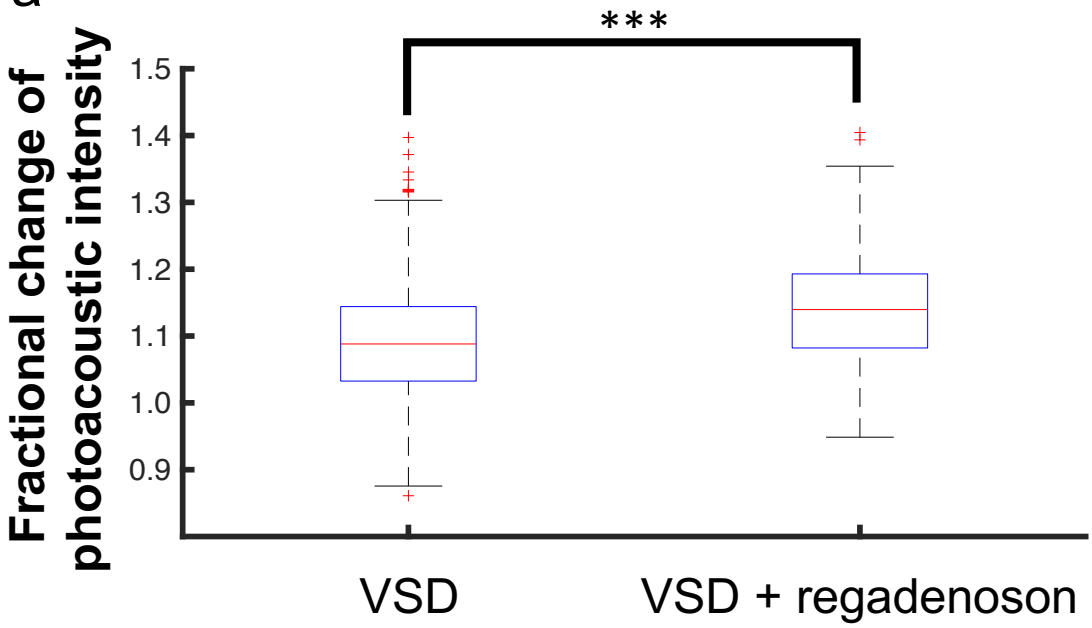


b

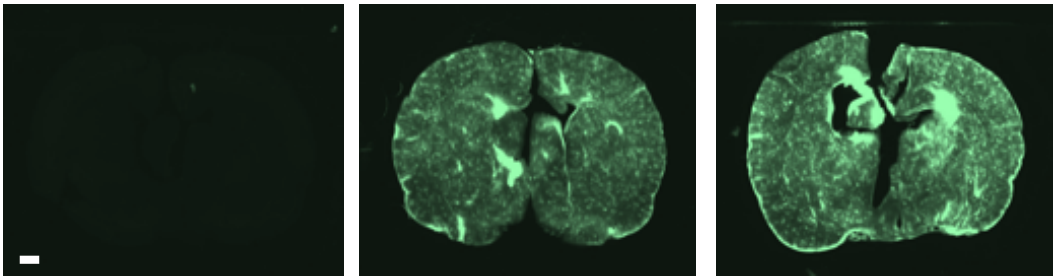

**Negative control:** VSD **(−)**, Lexiscan **(−)**

**Control:** VSD **(+)**, Lexiscan **(−)**

**BBB opening:** VSD **(+)**, Lexiscan **(+)**

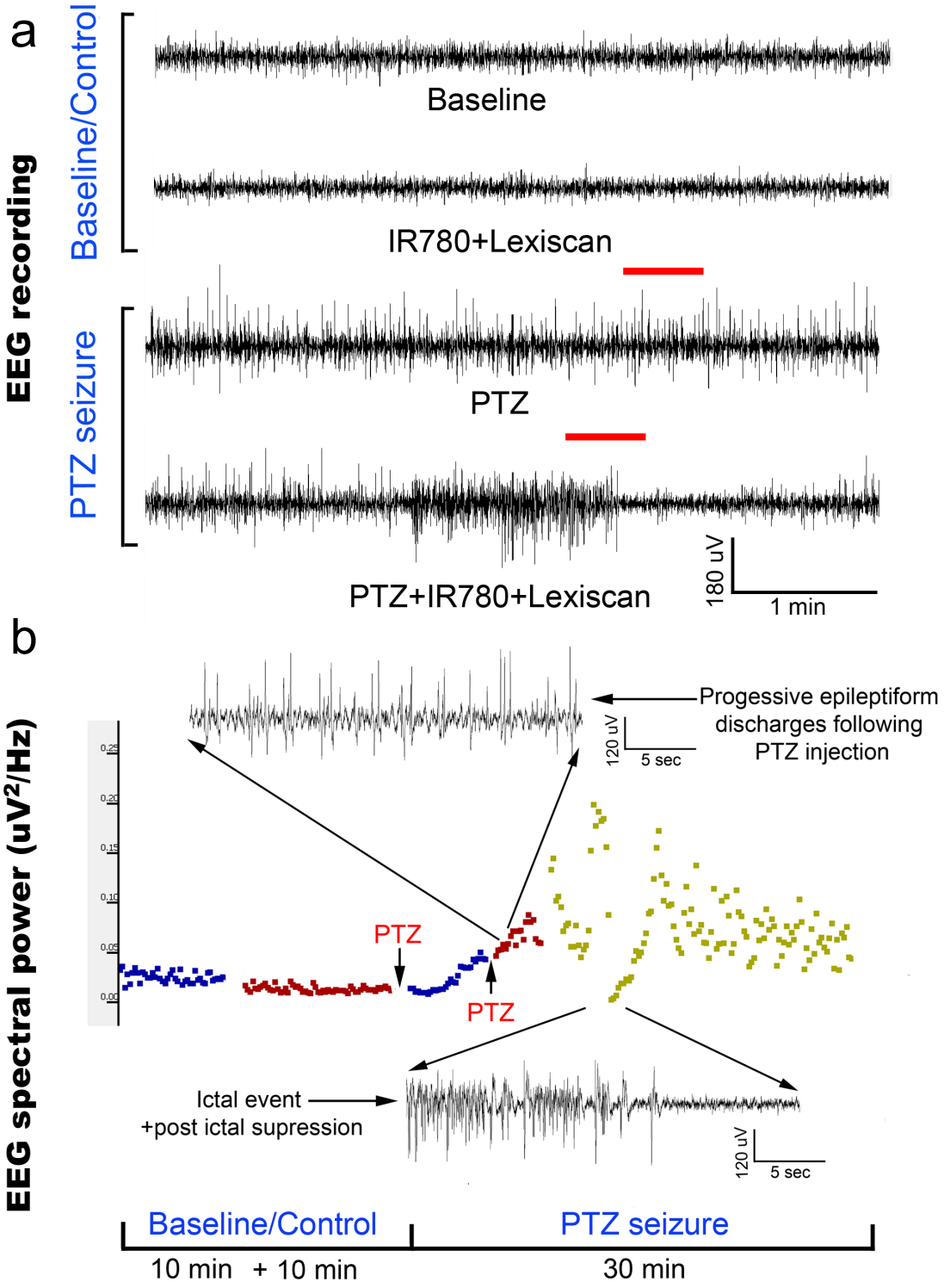
a
EEG recording
Baseline/Control
Baseline
IR780+Lexiscan
PTZ seizure
PTZ
PTZ+IR780+Lexiscan
180 uV
1 min
b
EEG spectral power (uV²/Hz)
Progessive epileptiform discharges following PTZ injection
120 uV
5 sec
PTZ
PTZ
Ictal event
+post ictal supression
120 uV
5 sec
Baseline/Control
PTZ seizure
10 min + 10 min
30 min

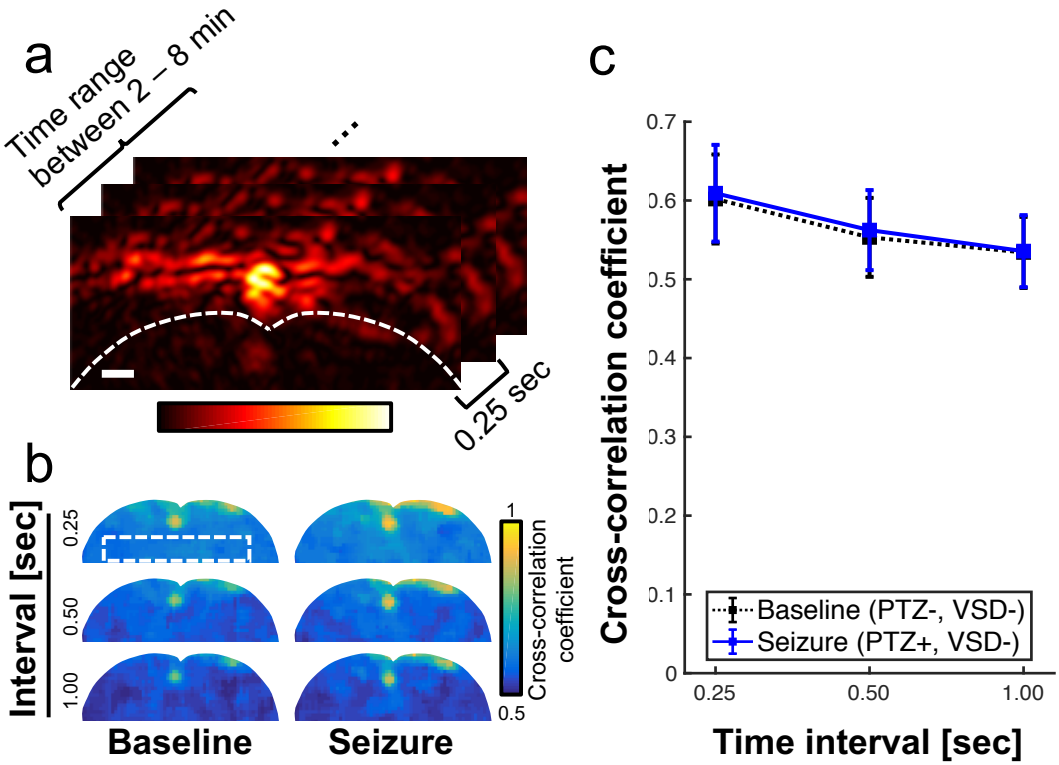
a
Time range between 2 – 8 min
0.25 sec
b
Interval [sec]
0.25
0.50
1.00
Baseline
Seizure
1
0.5
Cross-correlation coefficient
c
Cross-correlation coefficient
0.7
0.6
0.5
0.4
0.3
0.2
0.1
0
Baseline (PTZ-, VSD-)
Seizure (PTZ+, VSD-)
0.25
0.50
1.00
Time interval [sec]

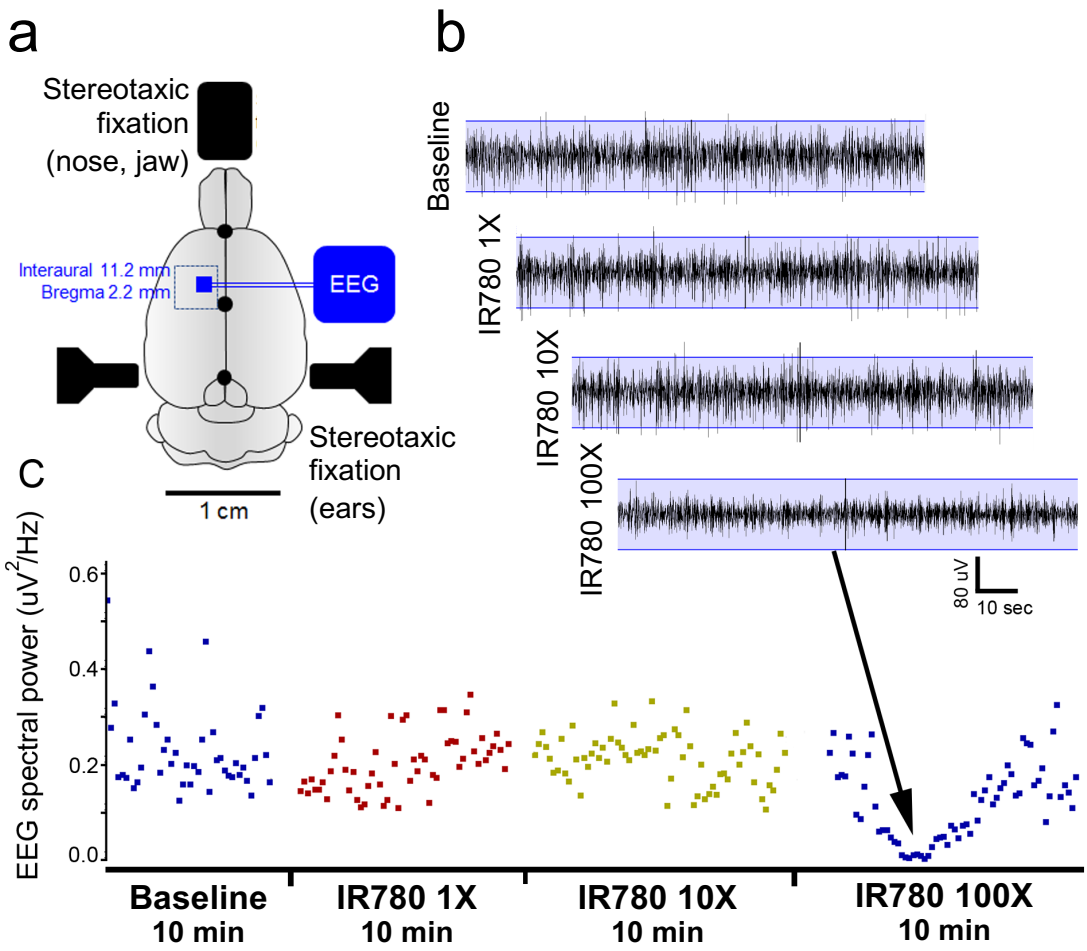
a
Stereotaxic
fixation
(nose, jaw)
Interaural 11.2 mm
Bregma 2.2 mm
EEG
Stereotaxic
fixation
(ears)
1 cm
b
Baseline
IR780 1X
IR780 10X
IR780 100X
80 uV
10 sec
c
EEG spectral power (uV²/Hz)
0.6
0.4
0.2
0.0
Baseline
10 min
IR780 1X
10 min
IR780 10X
10 min
IR780 100X
10 min